Bundling architecture in elastic filaments with applied twist

Amit Dawadi[†], Animesh Biswas[†], Julien Chopin[⋆], and Arshad Kudrolli[†]
[†] *Department of Physics, Clark University, Worcester, MA 01610, USA*
[⋆] *Instituto de Física, Universidade Federal da Bahia, Salvador-BA 40170-115, Brazil*
(Dated: June 23, 2025)

We investigate the formation of helical multifilament bundles and the torque required to achieve them as a function of applied twist. Hyperelastic filaments with circular cross sections are mounted parallel in a uniform circle onto end-clamps that can move along the twist axis depending on the applied axial load. With increasing twist, the filaments describe a hyperbolic hyperboloid surface before coming into contact in a circle, and then packing in a tight helical bundle in the center with increasing twist. While the bundle appears ordered for sufficiently small number of filaments, they are disordered for large enough number of filaments and applied twist. We reveal with x-ray tomography, that the packing of the filaments becomes disordered following a radial-instability which leads to a decrease in bundle radius, and migration of filaments relative to each other in the bundle. Nonetheless, the helical angle of the filaments in the bundle are found to be essentially constant, resulting in inclination angles which increase with distance from axis of rotation. We develop energy minimization analysis to capture the observed variations in bundle length and torque as a function of number of filaments considering the neo-Hookean nature of the filaments. We show that the bundle geometry and the applied load can be used to describe the non-linear torque profile measured as a function of twist angle.

I. INTRODUCTION

Twisted filaments can be found widely in organic and synthetic matter going back to antiquity [1]. They are an important element in fabricating metamaterials such as artificial spider silk with exceptional tensile strength, flexibility, and toughness [2, 3]. Slender fibers are spun together to not only gather them, but also increase their collective strength in making yarns as twisting increases the friction and mechanical interlocking between fibers [4–6]. However, making optimal yarns requires a deep understanding of their kinetics as it has been shown that yarn strength increases and then decreases with twist as competing factors cohesion and fiber inclination angle become dominant in the low and high twist regimes, respectively [7]. In the biological realm, collagen fibrils which bind muscle with bones through tendons and provide structural and mechanical support have been shown to have rope-like structure [8], and bundling and unbundling of flagellar filaments is important for the locomotion of Peritrichous bacteria [9]. Helical twist plays a role in stabilizing sickle cell disease causing sickle-hemoglobin macrofibers by determining their structural arrangement and energy landscape [10, 11]. Thus, functionalities of twisted filaments in biological systems [12], besides emerging applications such as in twistron energy harvesters [13], high efficiency twistocaloric coolers [14], and actuators in soft robotics [15–21], make them an important system to study.

While linear filaments with uniform circular cross sections can bundle tightly with hexagonal order when stacked together, it has long been realized that the packing grows disordered when they are twisted collectively since the filaments assume a helical shape with increasing curvatures as the filaments push out against each other [22]. The filament transects orthogonal to the axis of rotation become non-circular with increasing distance from axis of rotation and they can no longer close pack with the same hexagonal symmetry. Thus, the twisted packing structure of ropes and cables that optimize their strength and volume have been a subject of patents for well over a century. A mapping of the bundle cross section to a packing of disks on a non-Euclidean surface was introduced to describe the overall structure of the bundle with twist [23], and was tested with bendable but otherwise inextensible filaments [24].

However, elasticity plays a crucial role in the behavior of twisted filament bundles [25], affecting their order persistence [26] and promoting bundling through configurational instabilities and hydrodynamic interactions [27]. The effect of elasticity was recently investigated by measuring the torque required to twist hyperelastic filament pairs and comparing it with energy-based models [28]. Building on this research, we examine the packing, torque, and stored energy in multifilament bundles created by twisting initially parallel filaments that are initially held apart under constant tension. In contrast with previous studies [24, 26], we measure the torque required for bundle formation and present a combined geometric and energy-based model to describe bundle length and torque as a function of applied twist enabled by x-ray measurements of their internal structure.

The paper is organized as follows. We first discuss the experimental apparatus used to twist the filaments and measure its response using optical imaging and a torque sensor. Then, we discuss x-ray scanning to obtain and characterize the internal structure of the bundle. Based on these observations, we analyze the trends in the observed torque as a function twist angle and the evolving geometric parameters important to determining its magnitude. Then, we develop an elastogeometric model to explain overall growth of bundle length, energy stored,

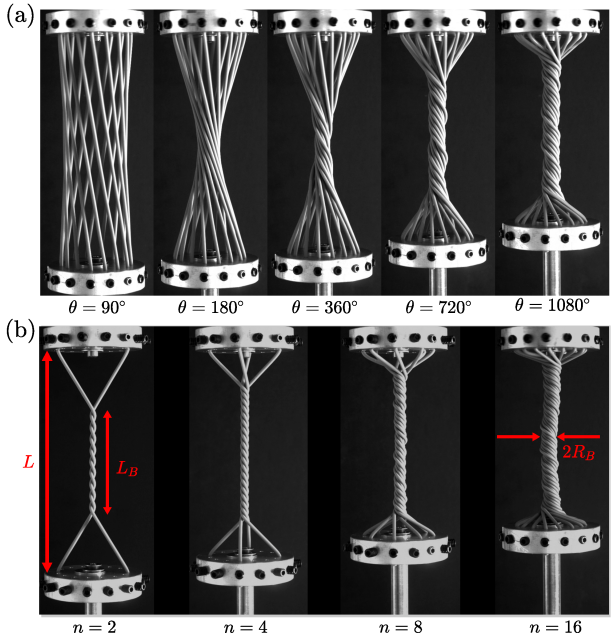

FIG. 1. (a) Formation of filament bundle with increasing applied twist angle θ ($L_0 = 162\,\text{mm}$; $n = 16$). Before filaments come in contact and form a bundle, they extend essentially linearly between their clamped ends. (b) The bundles observed with increasing number of filaments ($L_0 = 162\,\text{mm}$; $\theta = 1800°$). The clamp to clamp distance L, bundle length L_B and radius R_B used to characterize the evolving geometry of the system are indicated.

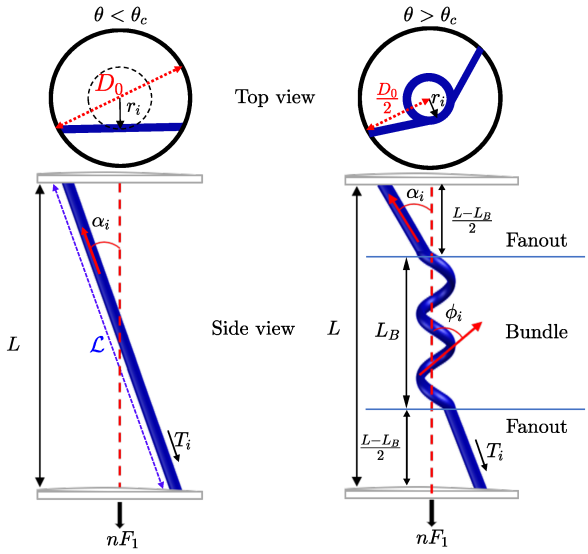

FIG. 2. A schematic representation of the geometry corresponding to a filament i before and after contact. The clamp to clamp distance is L and the curvilinear length of the stretched filament is $\mathcal{L}$. The angles the filaments subtend with the axis of twist while straight and in the helical bundle region are denoted by α_i and ϕ_i, respectively.

and torque with applied twist.

II. EXPERIMENTAL SYSTEM

The experiments are performed with silicone filaments obtained from MSC Industrial Supply that have been shown to be hyperelastic and can be modeled using a neo-Hookean constitutive law [28, 29]. They have circular cross sections with diameter $d_0 = 2.60\,\text{mm}$, Poisson's ratio $\nu \approx 0.5$, and shear modulus $\mu = 1.43 \pm 0.1\,\text{MPa}$ [28]. Their bundling mechanics is observed while varying the number of filament n between 2 and 16. The filaments are mounted symmetrically and in parallel onto two circular clamps with a diameter of $D_0 = 50\,\text{mm}$. These clamps are separated such that the relaxed length of the filaments between their clamped ends is $L_0 = 162\,\text{mm}$, with the filaments equally spaced by an angle of $360°/n$. The filaments are twisted by rotating one of the clamped ends with a Parker Motion Control system stepper motor through prescribed angle θ about the axis joining the centers of the two circular ends. The other clamped end is allowed to move along the twist axis with linear guides so that the distance between the clamps L can vary in response to the applied load F and the applied twist angle θ. The filaments consequently stretch and the resulting curvilinear length of a filament is represented by $\mathcal{L}$. The stretch factor λ is then given by, $\lambda = \frac{\mathcal{L}}{L_0}$, and the resulting diameter of the filament due to the resulting thinning of the filament due to volume conservation is given by $d = d_0/\sqrt{\lambda}$.

A load proportional to the number of filaments is applied at the moving end to taut the filaments, resulting in a total force $F = nF_1$, where $F_1 = 0.735\,\text{N}$. In practice we find that an additional frictional force F_μ associated with the linear guides can contribute to the axial load as we will discuss further while comparing our measurement with calculations. The applied load along the symmetry axis results in $\mathcal{L} = L_0 + \Delta L$, where $\Delta L = \frac{2F_1 L_0}{\pi\mu(1+\nu)d_0^2} \simeq 5.5\,\text{mm}$. We denote the resulting $\mathcal{L} = 167.5\,\text{mm}$ before application of twist as L_s because it is a convenient reference while discussing the further effect of applying twist.

Side view images obtained with a Pixelink camera are shown at various θ between 90° and 1080° for $n = 16$ in Fig. 1(a), and for $\theta = 1800°$ as n is increased from 2 to 16 in Fig. 1(b). We observe that the filaments tilt with respect to the axis of rotation, move inwards until they come in contact before θ reaches 180° at an angle θ_c, and then wrap around each other in the center as θ is increased further. Because of the applied load per filament is held constant, L decreases with increasing twist and number of filaments. After contact, the filaments form a bundle region at the center of length L_B, which grows towards the clamped ends with increasing twist. The bundles appear ordered in the case of $n = 2$ and 4, but disordered when $n = 8$ and $n = 16$ when $\theta = 360°$ or

higher in the examples shown. Further, incipient longitudinal buckling can be noted in the image corresponding to $n = 16$ at $\theta = 1800°$ as the bundle ends approaches the clamped ends. We confine our discussion to the bundling regime before the development of longitudinal buckling in this study.

III. GEOMETRIC ANALYSIS

A. Schematic of filaments with twist

A schematic representation of the progression of the overall geometry of a typical filament i before and after contact at angle θ_c is shown in Fig. 2. We represent the filament as being essentially straight and inclined with respect to the axis of twist by an angle α_i while $\theta \leq \theta_c$. We define the mean inclination angle $\alpha_f = \langle \alpha_i \rangle$, where $\langle .. \rangle$ represents averaging over the various filaments. Because of their symmetry, α_i and their closest distance of approach to the axis of twist r_i can be expected to be the same across the various filaments before contact, i.e., $\alpha_i = \alpha_f$. Then examining Fig. 2, we have $\alpha_f = \alpha_i = \sin^{-1}(\frac{D_0}{\mathcal{L}} \sin(\frac{\theta}{2}))$. When $\theta \approx 180°$, we have $\alpha_f = \sin^{-1}(\frac{D_0}{\mathcal{L}}) \approx 17.3°$. The corresponding tension $T_i = F_1/\cos\alpha_f$, results in an increase in length, $\Delta L = \frac{2F_1 L_0}{\pi\mu(1+\nu)d_0^2 \cos\alpha_f} \approx 5.76\,\text{mm}$, which is similar to the change in filament length estimated at $\theta = 0°$. Therefore, we assume for now that the filament length remains unchanged after the axial load is applied and before contact, i.e., $\mathcal{L} \simeq L_s$ for $0 \leq \theta \leq \theta_c$. Then,

$$\alpha_f = \sin^{-1}\left(\frac{D_0}{L_s}\sin\left(\frac{\theta}{2}\right)\right) \quad \text{for}\, \theta \leq \theta_c\,. \tag{1}$$

Above $\theta > \theta_c$, the filament is represented with linear segments inclined by α_i with respect to the axis of twist in the fanout regions between the clamps and where it comes in contact with the other filaments. In the bundle, the filament is represented as being helical while it is in contact with other filaments. The inclination angle of the filament in the bundle ϕ_i can be noted to be different from α_i in the fanout region because they can depend on r_i as we will reveal further using x-ray scanning. Examining Fig. 2, the filament inclination angle α_i for $\theta > \theta_c$ can be related to L, L_B, and r_i as,

$$\alpha_i = \tan^{-1}\left(\frac{\sqrt{D_0^2 - 4r_i^2}}{L - L_B}\right). \tag{2}$$

While L and L_B vary with θ, it is not possible to simplify and rewrite in terms of θ without further knowledge of the bundle structure.

B. Hyperboloid structure

If the filaments are straight while $\theta < \theta_c$ and have the same inclination angle, they can be expected to fall on a ruled surface which is a hyperbolic hyperboloid of one sheet [30]. An example, and the corresponding hyperboloid surface along with the cartesian coordinate system with z-axis aligned with axis of rotation is shown in Fig. 3(a). The projected boundary of the filaments when viewed perpendicular to the axis of twist should be a hyperbola. Fig. 3(b) shows comparisons of the projected edges of the filaments in the $x - z$ plane obtained by image processing for four different $\theta < \theta_c$. Good agreement can be observed confirming that the filaments fall on a hyperbolic hyperboloid surface and supporting the assumption that the filaments extend linearly from clamp to clamp while $\theta < \theta_c$.

C. Twist angle at contact

We can estimate θ_c which separates the observed hyperboloid and bundle regimes by noting that the filaments also extend essentially linearly between the clamped ends just as they come in contact. In the case of $n = 2$, the distance between filament centers is simply the filament diameter [28]. Because of the Poisson effect, the diameter after stretching d is somewhat lower than d_0, and given by $d_0/\sqrt{\lambda}$ for neo-Hookean filaments. Over the range $0 \leq \theta \leq \theta_c$, $\mathcal{L} \simeq L_s$, and thus $\lambda \simeq \frac{L_s}{L_0}$. Denoting diameter over this range as d_s, we have $d_s = d_0/\sqrt{\lambda} \simeq 2.5\,\text{mm}$. For larger n, the filaments come in contact in a circle with a radius R_c as shown in the inset to Fig. 3(c). Because the filaments are inclined, they touch along the long axis of their elliptical cross sections in the plane perpendicular to the twist axis. Then, the distance between contacts with neighbors is given approximately by $d_s/\cos\alpha_f$, and we have,

$$2\pi R_c = \frac{n d_s}{\cos\alpha_f}.$$

From the projected geometry of the filaments, we have $\cos(\frac{\theta_c}{2}) = \frac{2R_c}{D_0}$, and thus $\cos(\frac{\theta_c}{2}) = \frac{n d_s}{\pi D_0 \cos\alpha_f}$. Then, using Eq. (1), we have:

$$\cos\left(\frac{\theta_c}{2}\right) = \frac{n\, d_s}{\pi\, D_0 \sqrt{1 - \left(\frac{D_0}{L_s}\sin\left(\frac{\theta_c}{2}\right)\right)^2}} \text{ for } n > 2.$$

The resulting equation has to be solved numerically. We obtained θ_c by performing numerical integration and plot them (solid line) in Fig. 3(c).

Further, for $\theta_c \to 180°$, $\sin(\frac{\theta_c}{2}) \approx 1$, and $\sin\alpha_f \approx D_0/L_s$. In this case we have,

$$\begin{aligned} \cos\left(\frac{\theta_c}{2}\right) &\approx \frac{d_s}{D_0}\,, && \text{for } n = 2, \text{ and} \\ \cos\left(\frac{\theta_c}{2}\right) &\approx \frac{n d_s}{\pi D_0 \sqrt{1 - \left(\frac{D_0}{L_s}\right)^2}} && \text{for } n > 2. \end{aligned} \tag{3}$$

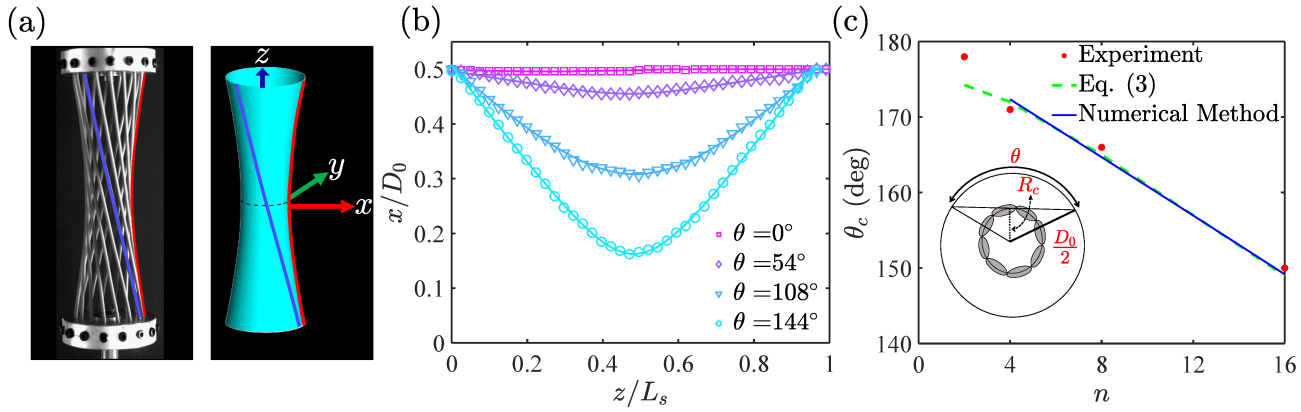

FIG. 3. (a) An image of the filaments with a representative filament denoted with a blue (gray) line ($n = 16$ and $\theta = 90°$). The bundle edge is also highlighted with a red (light gray) curve which corresponds to a hyperbola. The hyperbolic hyperboloid surface is mapped by rotating the curve about the z-axis. (b) The distance x from the tracked bundle edge to the twist axis is plotted as a function of the position along the z-axis at various θ. Each curve is described by a hyperbolic function. (c) The estimated and measured θ_c as a function of n which separates the hyperboloid and bundling regime ($L_0 = 162\,\text{mm}$). Inset: A schematic of the filaments geometry at central cross section as viewed along the twist axis for $\theta = \theta_c$ when filaments just come into contact. The filament cross sections are elliptical because of their inclination relative to the twist axis.

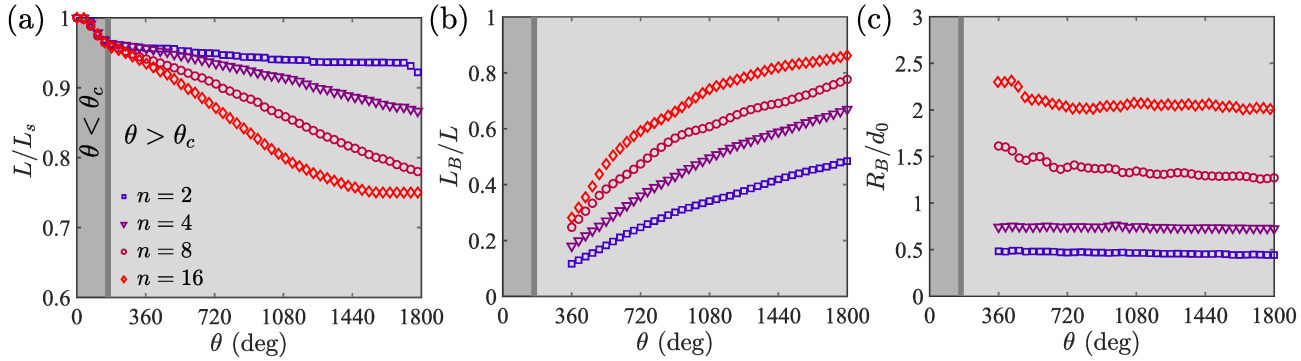

FIG. 4. (a) The clamp end to end distance L scaled by the pre-twist length L_s as a function of θ ($L_s = 167.5\,\text{mm}$). The rate of decrease of L is observed to change as the filaments come into contact around θ_c which is indicated by a vertical line. (b) The bundle length L_B increases after filaments come in contact and approaches L with increasing θ. (c) The bundle radius R_B scaled by filament diameter d_0 is essentially constant with increasing θ.

These approximate calculated values are plotted with dashed line in Fig. 3(c) and are consistent with the decreasing trend obtained numerically and by eye. We discuss the comparison of θ_c with those observed in the experiments obtained using torque measurements in Section VI.

IV. FILAMENT ASSEMBLY

We quantify the overall evolution of the filament assembly in terms of the end to end distance between the clamps L, the bundle length L_B and the bundle radius R_B. We obtain L by identifying the clamp edges from the images and plot it scaled by L_s in Fig. 4(a) as a function of θ for various n. The range of θ_c according to Eq. (3) are indicated for reference. Before contact, L/L_s can be observed to overlap and decrease with θ. Whereas, L/L_s can be observed to decrease at different rates depending on the number of filaments after contact. Although not quite as fast as before contact, the overall decrease can be observed to be faster for increasing n when $\theta > \theta_c$. For inextensible filaments, the decrease in distance is a consequence of the evolving geometry alone. However in the case of elastic filaments, a detailed calculation is necessary which we present in Section VII A.

While the bundle may be considered to form, starting from when the filaments first come in contact at $\theta = \theta_c$, the bundle length itself is difficult to measure from the side view images. Therefore, we plot L_B in Fig. 4(b) for $\theta > 360°$ when we can determine the length clearly by processing the images. Because of the uncertainty in accessing when filaments come in contact based on side-view images, the error in determining L_B is approximately $\pm 4\,\text{mm}$, $\pm 6\,\text{mm}$, $\pm 8\,\text{mm}$ and $\pm 10\,\text{mm}$ for $n = 2, 4, 8$ and 16, respectively. These errors nonetheless

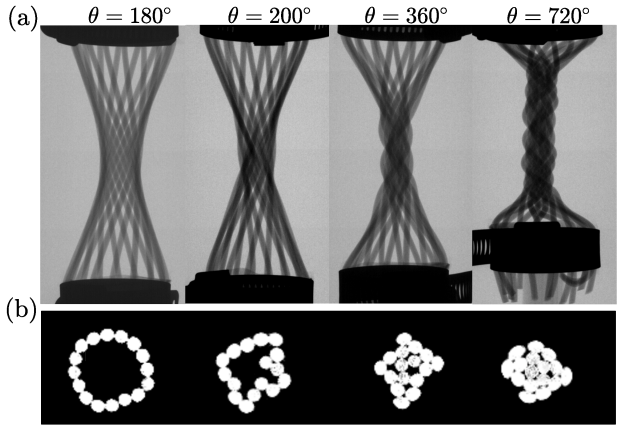

FIG. 5. (a) Radiograms of the bundle with increasing θ. (b) The corresponding central cross-sections obtained with Computed Tomography. The filaments start to come into contact in a ring at approximately $\theta_c = 140°$, and filaments undergo radial instability at $\theta \simeq 200°$. The filaments form a tight disordered bundle which grows in length with increasing twist ($L_s = 110\,\text{mm}$; $D_0 = 40\,\text{mm}$).

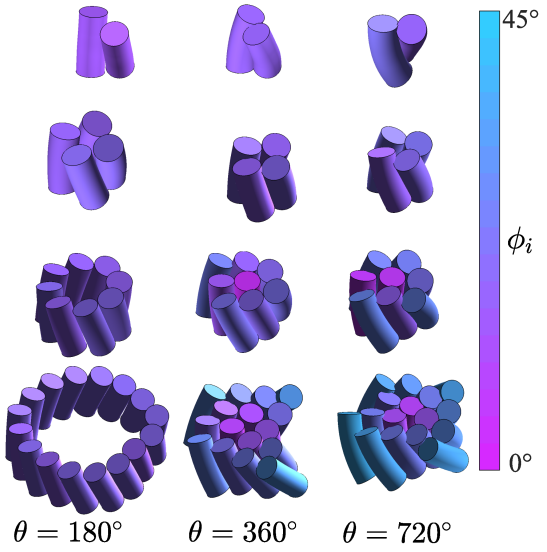

FIG. 6. The filament bundles ($n = 2, 4, 8, 16$) tracked in a central section of the bundle at $\theta = 180°$, 360°, and 720° with inclination angle ϕ denoted according to the color map. The filaments initially come in contact in a ring because they are mounted symmetrically at their ends on circular clamps and then make tight bundle after radial instability with further twist. The filaments have the same diameters but shown with decreasing magnification with n.

are much smaller compared to the change in L_B with n and θ. We observe that L_B increases rapidly after the filaments come in contact but slows down as it increases towards L. The bundle lengths for the same θ are systematically higher for greater n showing that the filaments not only wrap around each other but also push laterally against each other leading to a relatively greater L_B.

Complementarily, the bundle radius R_B can be also measured from the projection of the bundle cross section on the image plane after the filaments have wrapped around at least once. We obtain R_B by identifying the bundle edge from the images and subtracting filament radius to obtain the distance of the outmost filament from the axis of twist. Fig. 4(c) shows that R_B increases systematically with n. It can be also noted that R_B remains more or less constant, if not decreases slightly, for $\theta > 360°$, when it can be cleanly identified. Because filaments in the bundles incline with increasing twist, one may expect the radius to increase [23]. However, the filaments can stretch as the tension in the filaments increase with twist, which can lead the radius of individual filaments to decrease. The observation that the bundle radius remains essentially constant suggests that these two opposing effect appear to cancel each other in filament bundles formed under constant applied load conditions.

V. BUNDLE STRUCTURE

A. X-ray tomography

We perform x-ray scans to further reveal the internal structure of the filaments, and their arrangements at different cross-sections as they twist around each other and form the bundle. To fit the apparatus in the Varian BIR 150/130 Desktop CT system machine, we constructed a scaled down version of the apparatus with $D_0 = 40\,\text{mm}$ and $L_0 = 110\,\text{mm}$ to apply twist while using the same silicone filaments. Fig. 5 shows a set of radiograms and central bundle cross sections in the case of $n = 16$ as the bundles begin to form, after they buckle, and as the bundle grows and fills the entire length L with twist. We observe that the filaments are arranged symmetrically at $\theta = 180°$ well after coming in contact at $\theta_c \approx 140°$. As θ is increased further to 200°, the filaments are no longer arranged symmetrically.

Fig. 6 shows the rendering of an approximately 5 mm mid-section of the bundle for the different n with increasing θ. A similar order to disorder progression is observed for $n = 8$. However, the filaments remain ordered as they twist around each other in case of $n = 2$ and $n = 4$, and no rearrangements are observed over the range of twist angles investigated. Thus, while θ_c estimated using Eq. (3) are systematically lower for these bundles formed with $D_0 = 40\,\text{mm}$ versus the ones formed with $D_0 = 50\,\text{mm}$, the overall development of the bundles are observed to be similar in scaled down version.

We locate the centers of each of the filaments in the central cross section, and obtain the radius of gyration $R_g = \sqrt{\frac{1}{n}\sum_{i=1}^{n} r_i^2}$, the distance to the closest filament R_{min}, and the farthest filament R_{max} from the bundle center. These are scaled by d_0, and plotted for $n = 2, 4, 8$, and 16 in Fig. 7. In the case of $n = 2$, R_{min}, R_{max}, and

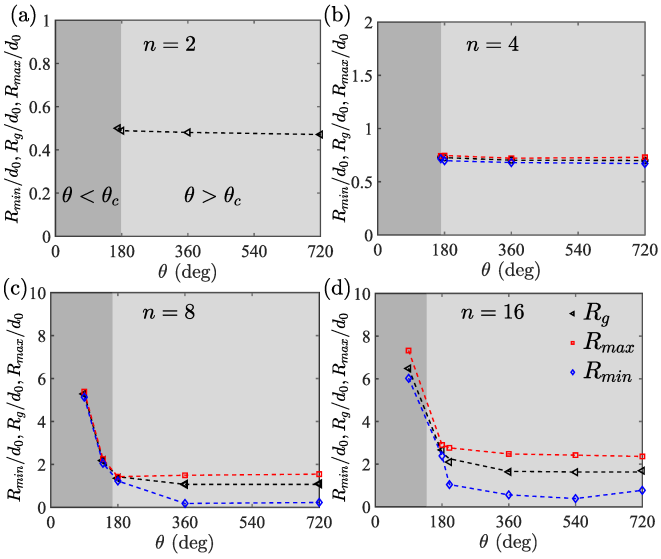

FIG. 7. R_g, R_{min} and R_{max} obtained from the filament positions tracked with x-ray tomography are normalized by d_0 and plotted as a function of applied twist ($D_0 = 40\,\text{mm}$; $L_s = 110\,\text{mm}$) for $n = 2, 4, 8$, and 16.

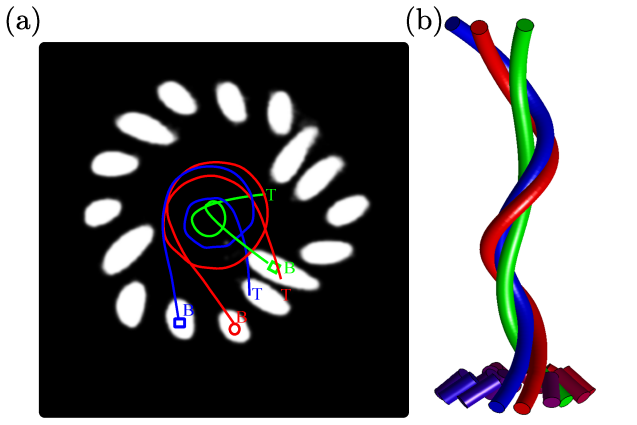

FIG. 8. (a) A cross section of the filaments in the fanout region between the clamped ends and the bundle ($n = 16$). The filament cross sections appear oblate because of their inclination. The projected position of the three representative filaments are also traced as viewed along the twist axis. The positions are obtained between the top (T) and the bottom (B) of the bundle shown in Fig. 5. (b) The tracked rendering of the three filaments. A short section of the other filaments are also rendered to indicate their initial position. The filaments can be noted to form helicoidal wrappings, but their distance from the center is observed to vary indicating that filaments migrate in the bundle as they wrap around the twist axis.

R_g are the same by definition. Further, they are also the same within filament mounting errors in the case of $n = 4$. This shows that they remain packed at the corners of a square, and do not undergo radial instability over the range of θ studied. However, R_g, R_{min} and R_{max} differ after the radial instability occurs and some of the filaments move towards the center in the case of $n = 8$ and 16. Just as we observed with optical imaging, we find that R_{max} remain essentially constant as the bundle length grows. Here, we further observe that and R_g remains essentially constant as well with increasing twist.

If the filaments were arranged in an ordered hexagonal lattice, the number of contacts n_c between filaments in a bundle cross section can be estimated to be 5, 14 and 33, for $n = 4, 8$ and 16, respectively. However, because a hexagonal packing cannot persist for large twist in tightly packed filaments with twist [23, 26], and the number of contacts decreases. Indeed, identifying contacts when the normal distance between neighboring filament centers is less than their diameter, n_c is typically found to be 4, 11, and 25 for $n = 4, 8$, and 16, respectively. Thus, the filaments move away from each other with increasing twist even as their diameter decreases as they are increasingly stretched. These two effects apparently offset each other leading the bundles to maintain their cross sectional radius with twist.

B. Bundle helicity

Figure 8(a) shows a cross section of the filaments in the fanout region between the bundle and clamped ends. While the filaments have circular cross sections, the cross sections in the slice perpendicular to the axis of rotation appear oblate because of their inclination relative to the twist axis. While all the filaments are clamped at their ends at a distance $D_0/2$ from the axis around which twist is applied, they enter the bundle at different distances from the twist axis after the development of radial instability. Thus, their inclination angle with respect to the axis of twist vary, and the ones which enters closer to the axis of twist appearing more oblate. The tracked centroid of the representative filaments are marked, and their projected positions as they twist around in the bundle and fanout at the other end are shown as continuous lines. A three-dimensional rendering of the tracked filaments is shown in Fig. 8(b), and an animated tracking of the filaments can be found in the supplementary documentation [31]. It can be seen from these tracked positions that the filaments do not maintain a constant helical radius along the entire length of the bundle. Thus, while the filaments appear to have an overall helical shape, they in fact migrate slowly in and out relative to each other from one end of the bundle to the other.

The migration in the filaments is observed in the bundles with $n = 8$ as well after a radial instability occurs. Thus, migration occurs when the filaments are brought together from some distance apart and then twisted around each other following a radial instability which leads to disordered packing. The relative migration of filaments has been noted in production of yarns [32–34], but was not observed in previous stud-

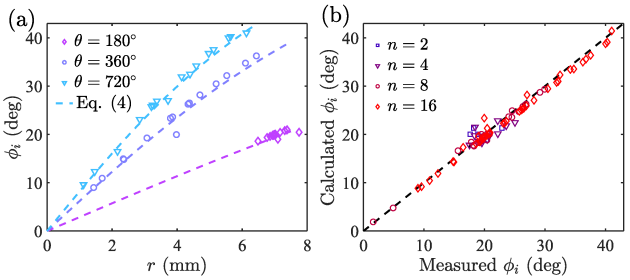

FIG. 9. (a) The angle of inclination of filaments ϕ_i as a function of distance from the axis of rotation r for $n = 16$ and $\theta = 180°, 360°$ and $720°$. Curves corresponding to Eq. (4) are also plotted and observed to be in good agreement with the data. (b) The measured and calculated ϕ_i using Eq. (4) for various θ and n are also in agreement as they fall close to the dashed line with unit slope. Filament migration leads to small deviations from the overall trends.

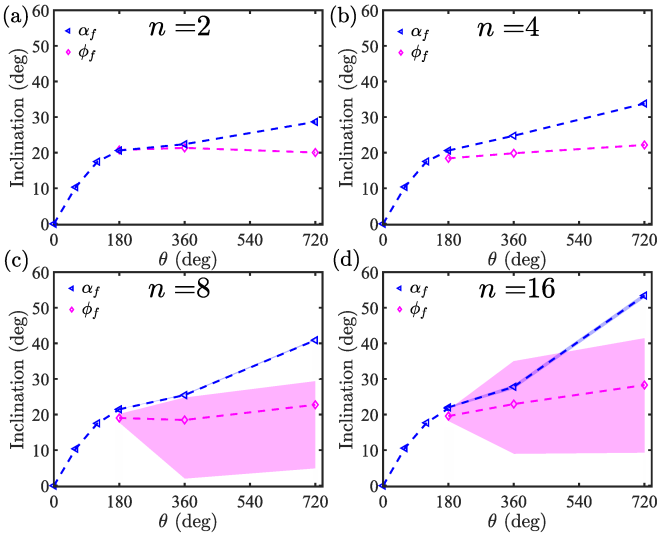

FIG. 10. (a-d) The average angle of inclination of the filaments in the fanout region α_f and in the bundle region ϕ_f obtained from x-ray CT measurements. The range of measured α_i and ϕ_i used to obtain α_f and ϕ_f are indicated by the shaded regions around the line joining points and can be observed to very narrow except in the case of inclinations angle in the bundle for $n = 8$ and 16.

ies when the filaments were hexagonally packed initially, and then twisted [24, 26]. The migration of the filaments may mitigate the dispersion in their extension of the filaments. This can lead the tension in the various filaments to equilibrate, rather than grow with filament distance from center of the bundle. Thus, the method by which the bundles are prepared have a significant effect on the bundle structure and the development of disorder.

C. Bundle region filament inclinations

We measure the angle of inclination of the filaments in the bundle ϕ_i relative to the axis of rotation from the tracked position of the filaments at the central cross section shown in Fig. 6. From the color bar it is clear that ϕ_i increase with increasing distance from the twist axis. We plot ϕ_i corresponding each filament i in Fig. 9(a) for three different θ in the 16-filament bundle. We observe that ϕ_i are clustered together when $\theta = 180°$ because the filaments are in a tight circle with a small dispersion in distance from the bundle center r. With increasing θ, a wider range of ϕ_i can be observed as some filaments approach the axis of twist after the development of the radial instability.

If a filament has a helical shape, then the filament tilt angle w.r.t. axis of rotation ϕ_i is given by $\phi_i = \tan^{-1}\left(\Omega_B\, r_i\right)$, where Ω_B is its helical angle [26] and r_i is the distance to the i^{th} filament from axis in the helical bundle. We estimate Ω_B by measuring the twist angle of the filament in the bundle $\Delta\theta = \theta - \theta_c$ and L_B, i.e. $\Omega_B = (\theta - \theta_c)/L_B$. Substituting, we get

$$\tan\phi_i = \frac{(\theta - \theta_c)}{L_B}\, r_i. \tag{4}$$

The inclination angle ϕ_i obtained from Eq. (4) are shown in Fig. 9(a) as dotted lines for the three different twist angles after contact. The error in determining L_B leads to some dispersion in estimating ϕ_i, but these are found to be less than the marker size. A comparison of measured and estimated ϕ_i for each filament with Eq. (4) are shown in Fig. 9(b) corresponding to various combinations of n and θ. Good overall agreement is observed which tells us that the inclination angle of the filaments in the bundle are mostly determined by their distance from the axis of the bundle and the overall twist applied to the bundle.

As we noted in the discussion of Fig. 8, the filaments migrate as they move from one end of the bundle to the other and the helices they form do not have a constant radii. This fact leads to some dispersion, but apparently the effect is small according to our measurements compared with the overall increase in ϕ_i with distance from the central twist axis.

D. Fanout region filament inclinations

We examine the inclination angles of the filaments in the fanout region and their relation to the inclination angles of the filaments in the bundle. Figure 10(a-d) shows a plot of measured angles α_f with markers and range of observed α_i with a shaded area for $n = 2, 4, 8$ and 16, respectively. α_f can be observed to increase similarly for the various n while $\theta \leq \theta_c$. After contact, α_f increase slowly compared with before contact in all cases. Further, α_f is observed to increase comparatively more rapidly with n. In the case of $n = 2$ and 4, r_i and α_i, are all the same for all the filaments because of their packing is

observed to be symmetric, i.e $\alpha_i = \alpha_f$. Although α_i in principle are not all the same for $n = 8$ and 16 after the radial instability because of variations in r_i, we find that in practice α_i is fairly narrowly distributed around their mean value $\alpha_f = \langle \alpha_i \rangle$ because $r_i \ll D_0$ in Eq. (2).

Figure 10(a-d) also shows the average inclination angle of the filaments in the bundle defined as $\phi_f = \langle \phi_i \rangle$, where $\langle .. \rangle$ indicates averaging over filaments in the bundle. Considering that the bundles are ordered and r_i are the same in the case of $n = 2$ and 4, $\phi_f = \phi_i$. However, ϕ_i are widely dispersed in the case of $n = 8$ and 16 as was shown in Fig. 9. Accordingly, we denote the range of ϕ_i which is bounded above corresponding to the outermost layer, i.e., $r_i = R_{max}$, and below by a filament which corresponds to $r_i = R_{min}$ in the case of $n = 8$ and 16. We observe that while ϕ_f and α_f are similar when $\theta \approx \theta_c$ in the case of all n, ϕ_f grows relatively slowly with increasing θ in comparison with α_f.

Such a divergence in the growth and dispersion of the angles can be understood from the fact that as L_B grows to approach L, then α_f will approach 90°. Whereas, ϕ_i cannot exceed an angle given by $\tan^{-1}(\Omega r_i)$ because of normal contact forces between filaments. For example, in the ordered case of $n = 2$, if $r_i \approx d_s/2$, then the maximum $\phi_f \to 57.5°$. The system can accommodate higher ϕ_i by pushing the filaments outward leading to changes in the packing structure and disorder, but this appears to occur beyond the range of θ investigated in our study.

VI. APPLIED AXIAL TORQUE

We now examine the consequences of the formation and evolution of the bundle on the torque needed as a function of applied twist. Figure 11(a) shows the applied torque M measured as a function of θ with a Mark-10 digital torque gauge. A rapid increase to a peak M_{peak} and then decrease is observed before the filaments come in contact. Such a peak has been noted previously in twisted filament pairs [28], where it was explained as arising as a consequence of the tension along the filaments pointing increasingly towards the axis of rotation as θ increases from 90° to θ_c. Then, M continues to rise in an increasingly non-linear fashion with θ for various n after contact.

The first minima in M encountered after M_{Peak} can be used to identify contact more clearly than in the plot of L versus θ, where a continuous change in its slope is observed. We plot θ_c obtained with this clear measurement in Fig. 3(c), and note that it is well described by the estimate given by numerical calculations and by Eq. (3).

A small but rapid decrease in M is also observed after contact at an angle θ_r before it increases non-linearly. Observing the bundle structure, we found a rearrangement of the filaments relative to each other after coming in contact in a uniform circle at θ_c. Consequently, we understand that the second decrease in M occurs due to a radial instability analogous to a buckling instability observed in twisted ribbons [35], where the ribbons were observed to fold along their length leading to a decrease in bundle radius and torque. In the case of $n = 16$, this angle $\theta_r = 194°$. (A small decrease for the same reason should also occur in the case of $n = 8$, but it is apparently small compared to experimental noise.)

Alternatively, the torque evolution with θ can be obtained from the geometry of the filament structure and the applied axial force. We note that each filament denoted with index i applies a torque which depends on its tension T_i, the angle it makes with axis of rotation α_i, and the distance of closest approach r_i to the axis around which twist is applied. Accordingly, the analysis can be conducted when the filaments are straight till they just come in contact, and when the filaments form a bundle after contact. From the schematic shown in Fig. 2(a) for $\theta \leq \theta_c$, $r_i = \frac{D_0}{2} \cos(\frac{\theta}{2})$. Thus,

$$M(\theta) = \frac{1}{2} \sum_{i=1}^{n} D_0 T_i \cos(\frac{\theta}{2}) \sin \alpha_i. \tag{5}$$

Combining the fact that for $\theta \leq \theta_c$, $\alpha_i = \alpha_f$, $T_i = F_1/\cos\alpha_f$, $F = nF_1$, and Eq. (1), we have

$$M(\theta) = \frac{1}{4} \frac{F D_0^2 \sin\theta}{\sqrt{\left({L_s}^2 - D_0^2 \sin^2(\frac{\theta}{2})\right)}} \text{ for } \theta \leq \theta_c. \tag{6}$$

After the formation of the bundle, i.e. $\theta > \theta_c$,

$$M(\theta) = \sum_{i=1}^{n} r_i T_i \sin \alpha_i, \tag{7}$$

where r_i is the radial distance from the twist axis where the filament i enters the bundle with angle given by Eq. (2).

Depending on the degree of stretching of each filament i, force balance along the twist axis gives us

$$F = \sum_{i=1}^{n} T_i \cos \alpha_i \,, \tag{8}$$

where T_i depends on the degree of stretching of the individual filament which can depend on their location relative to the twist axis. Because we observe significant migration of the filaments which leads to an averaging effect on stretching, we assume that the stretching is roughly the same, and the tension in the filaments, $T_i = \frac{F}{n \cos\alpha_i}$. Thus,

$$M(\theta) = \frac{F}{n} \sum_{i=1}^{n} r_i \tan \alpha_i. \tag{9}$$

Substituting Eq. (2), we get

$$M(\theta) = \frac{F}{L - L_B} \frac{1}{n} \sum_{i=1}^{n} r_i \sqrt{D_0^2 - 4r_i^2}. \tag{10}$$

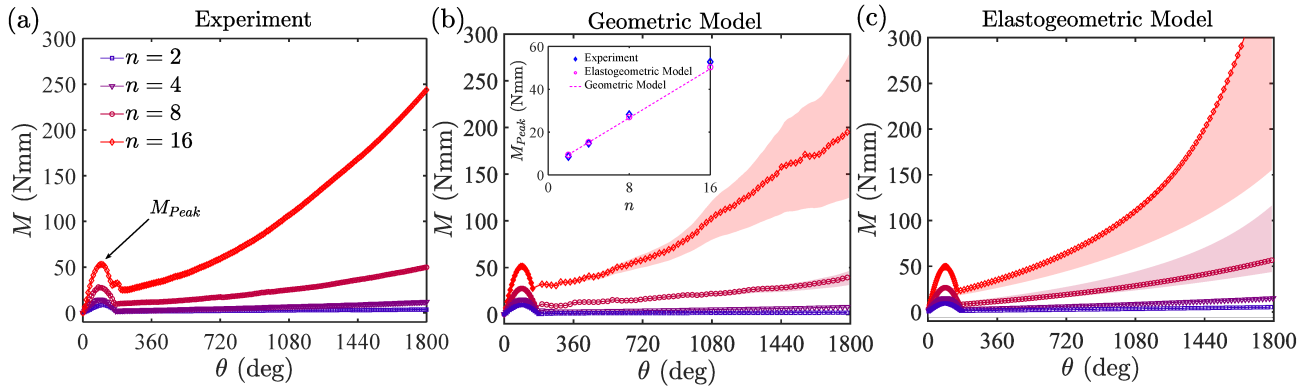

FIG. 11. (a) The axial torque measured with a torque sensor for various n. The peak torque M_{Peak} before contact is denoted. (b) The torque obtained using Eq. (6), and Eq. (12) corresponding to $\theta \leq \theta_c$ and $\theta > \theta_c$, respectively ($\beta = 1$). The shaded regions represent the uncertainty in the estimated torque due to the uncertainty in the measurment of L_B. Inset: M_{Peak} versus n measured and estimated using the geometric model and the neo-Hookean model are in good agreement after accounting for the sliding friction of the linear guides ($F_\mu = 1\,\mathrm{N}$). (c) The torque obtained with the elastogeometric model for various n captures the overall trends. The markers represent the estimate with R_e corresponding to the measured R_B, and the shaded regions represent the estimated range while using $R_e = R_g$ and $R_e = R_{max}$.

Now, for the tight bundle where $(r_i/D_0)^2 \ll 1$,

$$M(\theta) \approx \frac{FD_0}{L - L_B} \frac{1}{n} \sum_{i=1}^{n} r_i. \tag{11}$$

If we assume that the average is proportional to the bundle radius, i.e., $\frac{1}{n}\sum_{i=1}^{n} r_i = \beta R_B$, where $0 < \beta \leq 1$ depends on the filament packing, we have

$$M(\theta) = \frac{\beta F D_0 R_B}{L - L_B} \quad \text{for } \theta > \theta_c. \tag{12}$$

Using Eq. (6) and Eq. (12) with measured values of L, L_B, and R_B, we can obtain M using this geometric model plotted in Fig. 11(b). In the case of $n = 2$ and $n = 4$, $\beta = 1$ because the packing is symmetric and all filaments are at the same distance from axis of twist. In the case of $n = 8$ and 16, it is difficult to calculate the packing because of its disordered nature, and we plot the estimate with $\beta = 1$ corresponding to the upper bound to avoid introducing fitting parameters. The measured values of $\beta = 0.76$, and 0.63 for $n = 8$ and 16, respectively, from the x-ray scanning which gives a systematically lower estimate. The difference may be due to the assumption that the tension is the same, or the simplified geometry considered in the model. Nonetheless, similar overall features and relative increase in M with n are observed, illustrating the importance of the evolving bundle geometry and the axial load in determining the main trends in torque.

As noted in the discussion of the experimental apparatus, friction in the sliders on which the end clamps are mounted are found to increase F, i.e. $F = nF_1 + F_\mu$. Assuming a small offset value $F_\mu = 1\,\mathrm{N}$, we find quantitative agreement between the increasing M_{Peak} obtained using these two approaches to determining torque with experimental measurements (see Inset to Fig. 11(b)).

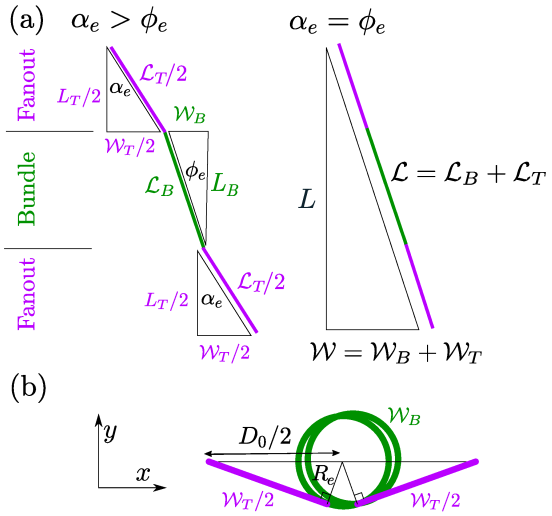

FIG. 12. (a) A schematic of the filament model where the shape of an effective twisted filament is projected onto a plane. The inclination angle of the filament in the bundle and fanout regions are different and depends on their distance from the twist axis. A complementary sketch of the model filament where the angle of inclination in the bundle and the fanout regions are approximated to be the same to simplify the analysis. (b) The projected view of the model filament in the xy-plane showing the fanout regions as straight segments and the helical bundle region as circles.

VII. ELASTOGEOMETRIC MODEL

A. Energy Analysis

We next use an energy minimization approach considering the elasticity of the filaments and the energy stored as a function of applied twist and load to describe

the main features of the bundle. We assume uniform stretching of the filaments, and thus uniform λ, along their length and among each other to simplify the calculation. The assumption is well justified in the case of $n = 2$ and 4, because of symmetry and previous observations with twisted pairs [28], and to some extent in $n = 8$ and 16 case as well based on the observation of filament migration which redistributes the tension and attenuates its systematic increase in the outer layers relative to the inner layers. In general, the total elastic energy E_{el} of the bundle is given by

$$E_{el} = E_s + E_t + E_b + E_c, \tag{13}$$

where E_s is the stretching energy, E_t the twisting energy, E_b the bending energy, and E_c the contact energy. The total axial force and the torque can be obtained from the total elastic energy by taking appropriate derivative with respect to L and θ, respectively:

$$F = \frac{\partial E_{el}}{\partial L}\Big|_{\theta}, \tag{14}$$

and

$$M = \frac{\partial E_{el}}{\partial \theta}\Big|_{L}. \tag{15}$$

A representative single filament is used to capture the overall shape of the filaments before and after contact, and a mean-field approach is used to consider a simplified picture of the contact interactions between filaments. A projected view of the filament is shown in Fig. 12(a). Before contact, the filaments are essentially straight and fall on the hyperboloid surface as discussed in Section III B. After contact, the geometry of the filaments is modeled in the bundle as a helix of effective radius R_e and curvilinear length $\mathcal{L}_B$ and in the fanout regions as straight lines of length $\mathcal{L}_T$ with $\mathcal{L} = \mathcal{L}_B + \mathcal{L}_T$. Accordingly, the filament will have inclination in the straight and helical regions angles α_e and ϕ_e, respectively. In the case of ordered bundle as in $n = 2$ and 4, α_e, and ϕ_e correspond to $\langle\alpha_i\rangle$, and $\langle\phi_i\rangle$ because the inclination angles in symmetric bundles are the same. However, in the cases of disordered bundles, i.e. $n = 8$ and 16, this is not the case.

In Section VI, we assumed the filament curvilinear length $\mathcal{L}$ remained unchanged while the filaments were twisted up to θ_c to estimate torque. Here, we calculate it using the elastic energy minimization approach not only for $\theta < \theta_c$, but also as θ is increased above θ_c using the neo-Hookean constitutive model [36]. The stretching energy for uniaxially stretched filaments is given by [28]:

$$E_s = \frac{n}{2}\mu V\left(\lambda^2 + \frac{2}{\lambda} - 3\right), \tag{16}$$

where $V = \frac{1}{4}\pi d_0^2 L_0$ is the unstressed volume of a filament.

As illustrated in Fig. 12(b), the projected length of the total curvilinear length of the filament on to the $x - y$ plane in the bundle and the fanout regions are denoted by $\mathcal{W}_B$ and $\mathcal{W}_T$, respectively. Then, according to Fig. 12(a), $\mathcal{L}_B = \sqrt{L_B^2 + \mathcal{W}_B^2}$ and $\mathcal{L}_T = \sqrt{(L - L_B)^2 + \mathcal{W}_T^2}$, and we have

$$\mathcal{W}_B = R_e(\theta - \theta_c), \tag{17}$$

and

$$\mathcal{W}_T = \sqrt{D_0^2 - 4R_e^2}. \tag{18}$$

Thus, the total projected length $\mathcal{W} = \mathcal{W}_B + \mathcal{W}_T$ reads,

$$\mathcal{W} = R_e(\theta - \theta_c) + \sqrt{D_0^2 - 4R_e^2}, \quad \text{for } \theta > \theta_c. \tag{19}$$

As modeled, the bundle length L_B is a parameter that can be set by imposing a stationary condition on the total energy with respect to L_B for a given L, i.e. $\frac{\partial E_{el}}{\partial L_B}\Big|_L = 0$. Then, $\frac{\partial E_{el}}{\partial L_B} = \frac{\partial E_{el}}{\partial \lambda}\frac{\partial \lambda}{\partial L_B} = 0$. Because $\lambda = \frac{1}{L_0}(\mathcal{L}_B + \mathcal{L}_T)$, we have $\frac{\partial \lambda}{\partial L_B} = \frac{1}{L_0}\left(\frac{L_B}{\mathcal{L}_B} - \frac{L_T}{\mathcal{L}_T}\right)$. Noting $\cos\alpha_e = \frac{L_T}{\mathcal{L}_T}$, and $\cos\phi_e = \frac{L_B}{\mathcal{L}_B}$, we have,

$$0 = T\left(\cos\alpha_e - \cos\phi_e\right), \tag{20}$$

where $T = \frac{1}{L_0}\frac{\partial E_{el}}{\partial \lambda}$ is the tension along the filament. Thus, $\alpha_e = \phi_e$, and Eq. (20) can be interpreted as a force balance along the filament.

The bending energy is given by [37]:

$$E_b = \frac{3n}{2}\mu I \kappa^2 \frac{\mathcal{L}_B}{\lambda}, \tag{21}$$

where $I = \frac{\pi}{64}d_0^4$ is the second moment of inertia, and κ is the curvature of the filament. Because filaments are assumed to be straight in the pre-contact regime, $E_b = 0$. After contact, the filament curvature $\kappa = 0$ in the fanout region, and the bending energy in that region is therefore zero. Whereas in the bundle where the filament is helical, $\kappa = \frac{1}{R_e}\frac{\tan^2\phi_e}{1+\tan^2\phi_e}$ [28]. Then, using trigonometric identities, we have

$$\kappa = \frac{1}{R_e}\left(\frac{\mathcal{W}_B}{\mathcal{L}_B}\right)^2. \tag{22}$$

From Fig. 12, one can note that

$$\mathcal{L}_B = \mathcal{L}\frac{\mathcal{W}_B}{\mathcal{W}}, \text{ for } \theta > \theta_c. \tag{23}$$

Substituting Eq. (23) into Eq.(22), we have

$$\kappa = \frac{1}{R_e}\left(\frac{\mathcal{W}}{\mathcal{L}}\right)^2 \text{ for } \theta > \theta_c, \tag{24}$$

and Eqs. (17), (23), and (24) into Eq. 21, we have for $\theta > \theta_c$,

$$E_b = \frac{3n}{8}\mu V\left(\frac{d_0}{2R_e}\right)^2\left(\frac{\mathcal{W}}{L_0}\right)^3\frac{R_e(\theta - \theta_c)}{L_0}\frac{1}{\lambda^4}. \tag{25}$$

Assuming that the twist is homogeneously distributed along the filament, the twisting energy is given by [36],

$$E_t = \frac{n}{4}\mu V \left(\frac{d_0\theta}{2L_0}\right)^2 \frac{1}{\lambda}. \tag{26}$$

Calculating the contact energy E_c stored in the bundle is difficult because of the complex geometry of contact in a twisted bundle. Building on the Hertz contact energy of two parallel cylinders in contact [38], an estimate of the contact energy for two filaments that are uniformly twisted around each other was obtained by balancing the inward force with bending [28]. If we consider all the contacts n_c between filaments in a bundle cross section are similar, then an estimate of the total contact energy stored in the bundle can be obtained by multiplying the estimate obtained previously for a single line contact by n_c. Thus,

$$E_c = \frac{1}{2}\ n_c\mu V \left(\lambda^2 - \frac{1}{\lambda}\right)^2 \left(\kappa\frac{d}{2}\right)^2 \frac{\mathcal{L}_B}{\mathcal{L}}, \tag{27}$$

which after substituting Eq. (23), Eq. (17) and $d = d_0/\sqrt{\lambda}$ give us,

$$E_c = \frac{1}{8}\ n_c\mu V\kappa^2 {d_0}^2 \frac{R_e(\theta-\theta_c)}{\mathcal{W}} \left(\lambda^{3/2} - \frac{1}{\lambda^{3/2}}\right)^2. \tag{28}$$

The total energy E_{el} is obtained by adding each contribution according to Eqs. (16), (25), (26), and (28) over the entire range of θ, while noting that $E_b = E_c = 0$ for $\theta \le \theta_c$. Because $\mathcal{W}$ given by Eq. (19) is a function of θ and R_e, E_{el} is a function of λ, θ, and R_e.

B. Stored elastic energy

To examine trends in the stored energy with n and θ, we use the experimentally measured, nearly constant values of R_B, shown in Fig. 4(c), in place of R_e; i.e. $R_e/d_0 = 0.44$, 0.72, 1.27, and 2.0 for $n = 2$, 4, 8, and 16, respectively. Then, λ is obtained numerically using the condition given by Eq. (14). The calculated λ is then used to evaluate E_s, E_b, E_t, E_c, and E_{el} as a function of θ. Examining the various components of the energy that contribute to the total elastic energy in Fig. 13, we observe that they change not only with θ, but also with n. In the case of $n = 2$, we observe that the contribution of stretching to the total energy does not change significantly with θ. This trend is different compared to the case examined in Ref. [28], where L was held constant, which resulted in a rapidly increasing E_s compared with other components. Here, we find that the contribution of E_t and then E_b increases relatively rapidly, while E_c is essentially negligible in the case of $n = 2$. While essentially doubling, the overall trends remain similar in the case of $n = 4$ with E_s increasing slowly, and E_b and E_t increasing rapidly with twist. However, we observe that

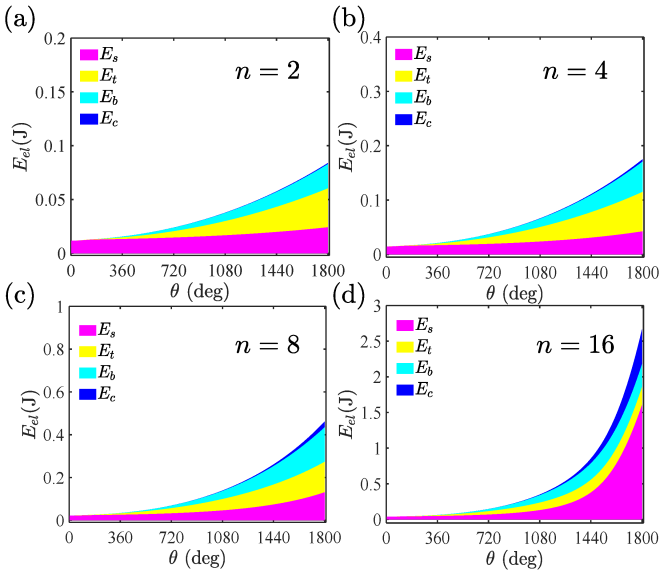

FIG. 13. (a-d) The elastic energy and the contributions due to filament stretching, twisting, bending, and contact, according to the elastogeometric model for $n = 2$ (a), $n = 4$ (b), $n = 8$ (c), and $n = 16$ (d). To avoid introducing additional free parameters, we use the measured values of n_c, and R_B for R_e.

E_s and E_c increases rapidly with increasing n as the filaments wrap around in a bundle. Consequently the total energy increases rapidly with twist in the case of $n = 8$ and $n = 16$, with E_s and E_c contributing an increasing fraction to the total energy.

C. Comparisons

In order to compare directly with measured quantities in our experiments, we obtain M as a function of θ using Eq. (15). The calculated ranges of torque for different n are plotted in Fig. 11(c) side by side with the measured values using the torque sensor in Fig. 11(a) and those estimated using the geometric model in Fig. 11(b). The curve shown with markers in Fig. 11(c) corresponds to E_{el} calculated using measured values of R_e, and $n_c = 1, 4, 11$, and 25 for $n = 2, 4, 8$, and 16, respectively. To test the importance of the choice of R_e and avoid using measured values, we further calculate M with R_e corresponding to R_g and R_{max} of an ordered hexagonal lattice. It can be noted that the overall trends are consistent with each other while comparing each n, although a somewhat faster rate of increase can be noted beyond $\theta = 1080°$ for $n = 16$, even after considering the range observed by considering various R_e. This may be expected as the simplification made in the filament geometry that the filaments in the fanout region are straight are increasingly not met.

The evolution of the bundle geometry can be also evaluated according to the elastogeometric model and com-

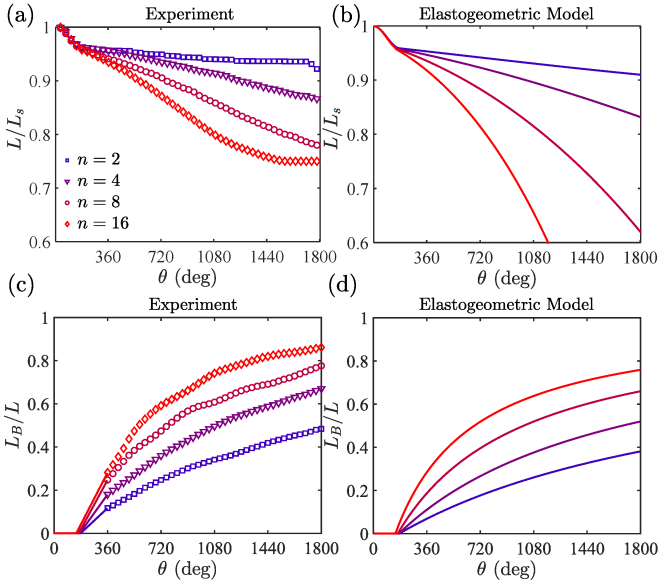

FIG. 14. (a,b) Comparison of L/L_s observed in the experiments and calculated using the elastogeometric model with R_e corresponding to experimentally measured R_B and $F_\mu = 1\,\mathrm{N}$. (c, d) Comparison of L_B/L observed in the experiments and calculated using the elastogeometric model. The overall trends are captured by the model, but systematic deviations grow with increasing n and θ.

pared with experimental trends. The clamp to clamp distance is given by

$$L = \sqrt{\mathcal{L}^2 - D_0^2 \sin^2\left(\frac{\theta}{2}\right)}, \quad \text{for } \theta \leq \theta_c. \tag{29}$$

and

$$L = \sqrt{\mathcal{L}^2 - \mathcal{W}^2}, \text{ for } \theta > \theta_c, \tag{30}$$

We also compare the measured and the calculated L scaled by L_s side by side in Fig. 14(a) and Fig. 14(b), respectively. Good description of the trends for $n = 2$ and 4 are observed. While the model captures the trends at lower θ, deviations grow as θ increases above 720° in the case of $n = 8$ and 16.

Further, the bundle length $L_B = \sqrt{\mathcal{L}_B^2 - \mathcal{W}_B^2}$ is evaluated using Eqs. (17) and (23). We plot the experimentally measured and estimated L_B scaled by L in Fig. 14(c) and Fig. 14(d), respectively. We note that the energy analysis yields overall good description of the trends. However, the elastogeometric model systematically underestimates L_B because of the geometric simplification needed to evaluate the model.

D. Discussion of discrepancy

The energy-based approach found that the filament inclination angles in twisted filament pairs have to be the same in the bundle and fanout regions to have equilibrium. In deriving this condition, we assumed that filaments in the fanout regions are well approximated by linear segments. While bending is visible near the clamps, we ignored this contribution as being small. Further it was assumed the transition of bending from the fanout region to the bundling region occurs abruptly. The fact that α_i increases more rapidly than ϕ_i indicates that this approximation increasingly beings to fail as the bundle length increases and the fanout region decreases.

Further, it is possible that inter-filament friction leads to some increase in α_i relative to ϕ_i. However, we added a lubricant between the filaments and found that it does not lead to a significant change in the bundle length. Changing the order of applied strain by twisting two filaments and then applying tension showed some hysteresis, but even in this case the angles remained different. However, when we increased the applied axial force F by an order of magnitude which leads to significantly greater filament stretching, we did find that α_i and ϕ_i approach each other. Since greater tension in the filaments leads to higher normal forces between twisted filaments, one may expect the effect of friction to persist if they are important. Hence, these observations appear to rule out friction as the explanation for the source of growing discrepancy.

Finally, it is possible that excluded volume effects which lead to additional contact forces between the filaments, along not only the radial direction considered here, but also along the axial direction, play an increasing role in the growing divergence with twist. Further analysis based on the direction in which inter filament forces act is needed, but is beyond the scope of our study.

VIII. CONCLUSIONS

In conclusion, by performing complementary optical and x-ray measurements we elucidated the formation of multifilament bundles as individual filaments are bought together and twisted. Guided by these observations we analyzed the measured torque required to form them, and developed an elastogeometric model to estimate the energy stored in the system considering the hyperelastic nature of the filaments. The overall trends in measured torque and contraction length with twist angle is observed. Good quantitative agreement is observed for sufficiently low twist angles, but systematic deviations are found to grow because of the simplified geometry of the bundle considered in calculating the energies. While advancing the understanding of the system and providing useful estimates of the energy stored and the mechanical nature of the system, our study nonetheless illustrates the complexity of filament bundling and the need for further investigation in concert with detailed numerical simulations of the bundle formation.

IX. ACKNOWLEDGMENTS

This work was supported under U.S. National Science Foundation grant DMR-2005090.

[1] J. Bohr and K. Olsen. The ancient art of laying rope. *EPL (Europhysics Letters)*, 93(6):60004, March 2011.

[2] Yuanyuan Dou, Zhen-Pei Wang, Wenqian He, Tianjiao Jia, Zhuangjian Liu, Pingchuan Sun, Kai Wen, Enlai Gao, Xiang Zhou, Xiaoyu Hu, Jingjing Li, Shaoli Fang, Dong Qian, and Zunfeng Liu. Artificial spider silk from ion-doped and twisted core-sheath hydrogel fibres. *Nature Communications*, 10(1):5293, 2019.

[3] Xiang Zhou, Shaoli Fang, Xueqi Leng, Zunfeng Liu, and Ray H. Baughman. The power of fiber twist. *Accounts of Chemical Research*, 54(11):2624–2636, 2021. PMID: 33982565.

[4] Antoine Seguin and Jérôme Crassous. Twist-controlled force amplification and spinning tension transition in yarn. *Phys. Rev. Lett.*, 128:078002, Feb 2022.

[5] Jesse M. Hanlan, Gabrielle E. Davis, and Douglas J. Durian. Twist and measure: characterizing the effective radius of strings and bundles under twisting contraction. *Soft Matter*, 19:4315–4322, 2023.

[6] Jérôme Crassous, Samuel Poincloux, and Audrey Steinberger. Metastability of a periodic network of threads: Shapes of a knitted fabric. *Phys. Rev. Lett.*, 133:248201, Dec 2024.

[7] P. Schwartz. *Structure and Mechanics of Textile Fibre Assemblies*. The Textile Institute Book Series. Woodhead Publishing, 2019.

[8] Laurent Bozec, Gert van der Heijden, and Michael Horton. Collagen fibrils: Nanoscale ropes. *Biophysical Journal*, 92(1):70–75, 2007.

[9] Nicholas C. Darnton, Linda Turner, Svetlana Rojevsky, and Howard C. Berg. On torque and tumbling in swimming *escherichia coli*. *Journal of Bacteriology*, 189(5):1756–1764, 2007.

[10] Lee Makowski and Beatrice Magdoff-Fairchild. Polymorphism of sickle cell hemoglobin aggregates: Structural basis for limited radial growth. *Science*, 234(4781):1228–1231, 1986.

[11] M. S. Turner, R. W. Briehl, F. A. Ferrone, and R. Josephs. Twisted protein aggregates and disease: The stability of sickle hemoglobin fibers. *Phys. Rev. Lett.*, 90:128103, Mar 2003.

[12] Natascha Leijnse, Younes Farhangi Barooji, Mohammad Reza Arastoo, Stine Lauritzen Sønder, Bram Verhagen, Lena Wullkopf, Janine Terra Erler, Szabolcs Semsey, Jesper Nylandsted, Lene Broeng Oddershede, Amin Doostmohammadi, and Poul Martin Bendix. Filopodia rotate and coil by actively generating twist in their actin shaft. *Nature Communications*, 13(1):1636, 2022.

[13] Shi Hyeong Kim, Carter S. Haines, Na Li, Keon Jung Kim, Tae Jin Mun, Changsoon Choi, Jiangtao Di, Young Jun Oh, Juan Pablo Oviedo, Julia Bykova, Shaoli Fang, Nan Jiang, Zunfeng Liu, Run Wang, Prashant Kumar, Rui Qiao, Shashank Priya, Kyeongjae Cho, Moon Kim, Matthew Steven Lucas, Lawrence F. Drummy, Benji Maruyama, Dong Youn Lee, Xavier Lepró, Enlai Gao, Dawood Albarq, Raquel Ovalle-Robles, Seon Jeong Kim, and Ray H. Baughman. Harvesting electrical energy from carbon nanotube yarn twist. *Science*, 357(6353):773–778, 2017.

[14] Run Wang, Shaoli Fang, Yicheng Xiao, Enlai Gao, Nan Jiang, Yaowang Li, Linlin Mou, Yanan Shen, Wubin Zhao, Sitong Li, Alexandre F. Fonseca, Douglas S. Galvão, Mengmeng Chen, Wenqian He, Kaiqing Yu, Hongbing Lu, Xuemin Wang, Dong Qian, Ali E. Aliev, Na Li, Carter S. Haines, Zhongsheng Liu, Jiuke Mu, Zhong Wang, Shougen Yin, Márcio D. Lima, Baigang An, Xiang Zhou, Zunfeng Liu, and Ray H. Baughman. Torsional refrigeration by twisted, coiled, and supercoiled fibers. *Science*, 366(6462):216–221, 2019.

[15] Moshe Shoham. Twisting wire actuator. *Journal of Mechanical Design*, 127(3):441–445, 07 2004.

[16] Márcio D. Lima, Na Li, Mônica Jung de Andrade, Shaoli Fang, Jiyoung Oh, Geoffrey M. Spinks, Mikhail E. Kozlov, Carter S. Haines, Dongseok Suh, Javad Foroughi, Seon Jeong Kim, Yongsheng Chen, Taylor Ware, Min Kyoon Shin, Leonardo D. Machado, Alexandre F. Fonseca, John D. W. Madden, Walter E. Voit, Douglas S. Galvão, and Ray H. Baughman. Electrically, chemically, and photonically powered torsional and tensile actuation of hybrid carbon nanotube yarn muscles. *Science*, 338(6109):928–932, 2012.

[17] Carter S. Haines, Márcio D. Lima, Na Li, Geoffrey M. Spinks, Javad Foroughi, John D. W. Madden, Shi Hyeong Kim, Shaoli Fang, Mônica Jung de Andrade, Fatma Göktepe, Özer Göktepe, Seyed M. Mirvakili, Sina Naficy, Xavier Lepró, Jiyoung Oh, Mikhail E. Kozlov, Seon Jeong Kim, Xiuru Xu, Benjamin J. Swedlove, Gordon G. Wallace, and Ray H. Baughman. Artificial muscles from fishing line and sewing thread. *Science*, 343(6173):868–872, 2014.

[18] Nicholas Charles, Mattia Gazzola, and L. Mahadevan. Topology, geometry, and mechanics of strongly stretched and twisted filaments: Solenoids, plectonemes, and artificial muscle fibers. *Phys. Rev. Lett.*, 123:208003, Nov 2019.

[19] Mehmet Kanik, Sirma Orguc, Georgios Varnavides, Jinwoo Kim, Thomas Benavides, Dani Gonzalez, Timothy Akintilo, C. Cem Tasan, Anantha P. Chandrakasan, Yoel Fink, and Polina Anikeeva. Strain-programmable fiber-based artificial muscle. *Science*, 365(6449):145–150, 2019.

[20] Shijun Wang, Ye Xiao, and Zhiping Xu. Energy-conversion efficiency and power output of twisted-filament artificial muscles. *Extreme Mechanics Letters*, 50:101531, 2022.

[21] Caterina Lamuta. Perspective on highly twisted artificial muscles. *Applied Physics Letters*, 122(4):040502, 01 2023.

[22] Gregory M. Grason. Colloquium: Geometry and optimal packing of twisted columns and filaments. *Rev. Mod. Phys.*, 87:401–419, May 2015.

[23] Isaac R. Bruss and Gregory M. Grason. Topological defects, surface geometry and cohesive energy of twisted filament bundles. *Soft Matter*, 9:8327–8345, 2013.

[24] Andreea Panaitescu, Gregory M. Grason, and Arshad Kudrolli. Measuring geometric frustration in twisted inextensible filament bundles. *Phys. Rev. E*, 95:052503, May 2017.

[25] Daria W. Atkinson, Christian D. Santangelo, and Gregory M. Grason. Mechanics of metric frustration in contorted filament bundles: From local symmetry to columnar elasticity. *Phys. Rev. Lett.*, 127:218002, Nov 2021.

[26] Andreea Panaitescu, Gregory M. Grason, and Arshad Kudrolli. Persistence of perfect packing in twisted bundles of elastic filaments. *Phys. Rev. Lett.*, 120:248002, Jun 2018.

[27] Yi Man, William Page, Robert J. Poole, and Eric Lauga. Bundling of elastic filaments induced by hydrodynamic interactions. *Phys. Rev. Fluids*, 2:123101, Dec 2017.

[28] Julien Chopin, Animesh Biswas, and Arshad Kudrolli. Energetics of twisted elastic filament pairs. *Phys. Rev. E*, 109:025003, Feb 2024.

[29] Raymond W Ogden. *Non-linear elastic deformations*. Courier Corporation, 1997.

[30] D. Hilbert and S. Cohn-Vossen. *Geometry and the Imagination*. Chelsea scientific books. Chelsea Publishing Company, 1952.

[31] See supplemental material at [url will be inserted by publisher] for further information on methods, movies and analysis.

[32] J.W.S. Hearle, P. Grosberg, and S. Backer. *Structural Mechanics of Fibers, Yarns, and Fabrics*. Number v. 1 in Structural Mechanics of Fibers, Yarns, and Fabrics. Wiley-Interscience, 1969.

[33] L. R. G. Treloar. 28—a migrating-filament theory of yarn properties. *Journal of the Textile Institute Transactions*, 56(7):T359–T380, 1965.

[34] J.W.S. Hearle, B.S. Gupta, and V.B. Merchant. Migration of fibers in yarns: Part i: Characterization and idealization of migration behavior. *Textile Research Journal*, 35(4):329–334, 1965.

[35] Julien Chopin and Arshad Kudrolli. Tensional twist-folding of sheets into multilayered scrolled yarns. *Science Advances*, 8(14), apr 2022.

[36] Ray W. Ogden. *Non-Linear Elastic Deformations*. Dover, New York, 1984.

[37] A. Ghatak and L. Mahadevan. Solenoids and plectonemes in stretched and twisted elastomeric filaments. *Phys. Rev. Lett.*, 95:057801, Jul 2005.

[38] Kenneth Langstreth Johnson. *Contact mechanics*. Cambridge university press, 1987.